Smart Structures and Systems, *Vol. 36, No. 2 (2025) 83-95*
https://doi.org/10.12989/sss.2025.36.2.083

Adaptive vibration control of smart hybrid nanocomposite reinforced the sport structures with machine learning – Optimized state-dependent damping

Guochen Zhang*[1] and Bing Lin [2]

[1] *School of Physical Education, Anyang Normal University, Anyang 45000, Henan, China*
[2] *School of Physical Education, Chongqing Preschool Education College, Chongqing 404047, China*

(*Received June 26, 2025, Revised August 9, 2025, Accepted August 14, 2025*)

Abstract. This study introduces a novel approach for vibration control in smart hybrid nanocomposite-reinforced sport structures, utilizing the Time-Delay Feedback Controller with Derivative Action (TDF controller with DA). The Carrera unified formulation (CUF) is employed to create a mathematical model that captures the dynamic behavior of these structures under high-impact and oscillatory forces. The TDF controller with DA incorporates time-delay feedback combined with derivative action to improve system stability and mitigate vibrations under dynamic loading. The hybrid nanocomposite material, comprising ZnO (zinc oxide), and GO (graphene oxide) enhances the mechanical and electromechanical properties of the sport structures, making them ideal for high-performance applications. Functionally graded nanocomposite face sheets, integrated with piezoelectric sensor-actuator layers, allow real-time adaptive control, dynamically adjusting damping characteristics in response to external disturbances. Rigorous simulations demonstrate that the TDF controller with DA outperforms traditional control methods, significantly reducing vibrations and enhancing dynamic stability. This research establishes a foundation for developing next-generation sport structures that offer superior resilience and longevity. The proposed approach shows great promise for improving the design and performance of sports equipment and infrastructure, particularly in environments with frequent high-impact forces.

Keywords: adaptive structures; carrera unified formulation; deep learning; hybrid nanocomposite; intelligent vibration control; sport structures; swarm intelligence

1. Introduction

Composite materials play a crucial role in modern engineering due to their superior mechanical properties and versatility (Ghadiri Rad and Hosseini 2024, Mir *et al*. 2024). These materials are composed of two or more distinct constituents, typically a matrix and a reinforcement, which synergistically enhance their overall performance (Abu Salem *et al*. 2025, Zhou *et al*. 2025). Engineers prefer composites for their high strength-to-weight ratio, making them essential in aerospace, automotive, and structural applications (Shi *et al*. 2025, Yan and Zhao 2025). The ability to tailor composite properties by varying fiber orientation, resin type, and manufacturing processes provides engineers with design flexibility (Daraei *et al*. 2024). Moreover, composites exhibit excellent corrosion resistance, extending the service life of structures and reducing maintenance costs (Ebrahimi and Dabbagh 2019). Their impact resistance and fatigue strength surpass many traditional materials, improving reliability in dynamic and high-stress environments (Ebrahimi and Reza Barati 2016). Advancements in composite technology enable the development of lightweight, high-performance structures while promoting sustainability (Sobhy and Alakel Abazid 2022). Bio-based and recycled composites contribute to environmentally friendly engineering solutions, aligning with global sustainability goals (Zhang *et al*. 2023). Additionally, composites facilitate innovation in additive manufacturing and 3D printing, expanding possibilities in custom and complex geometries (Hamzah *et al*. 2018). Despite these advantages, engineers must consider challenges such as material anisotropy, complex fabrication techniques, and repair difficulties (Li *et al*. 2019a). Computational modeling and simulation techniques help predict composite behavior, optimizing their performance in engineering applications (Li *et al*. 2019b). The integration of smart composites with embedded sensors enhances structural health monitoring and real-time performance assessment (Qin *et al*. 2019). Engineers also explore hybrid composites to achieve multifunctional properties that traditional materials cannot offer (Azmi *et al*. 2019). As research progresses, nanocomposites and advanced polymer matrix materials promise further improvements in strength, durability, and functionality (Al-Houri *et al*. 2024). Ultimately, composite materials represent a transformative area in engineering, enabling the creation of lightweight, durable, and high-performance structures across various industries (Ai and Gao 2017).

Systems with controllers are fundamental in

*Corresponding author, Ph.D.,
E-mail: guochenzhang@2980.com

ISSN: 1738-1584 (Print), 1738-1991 (Online)

engineering, enabling precise regulation and automation across various applications (Bauomy and El-Sayed 2020). Controllers enhance system stability, efficiency, and performance by adjusting inputs based on feedback mechanisms (Ghazi *et al*. 2022). Engineers utilize control systems in diverse fields such as robotics, aerospace, manufacturing, and process industries to optimize operations and ensure reliability (Ye *et al*. 2017). The integration of advanced controllers, including PID, adaptive, and intelligent control algorithms, allows for improved responsiveness and adaptability in dynamic environments (Zhang *et al*. 2024). As engineering systems grow more complex, the role of controllers becomes increasingly vital in achieving precision, safety, and efficiency in modern technological advancements (Warke *et al*. 2024).

Various structures are essential in engineering due to their ability to efficiently withstand loads while maintaining structural integrity (Zare *et al*. 2020, Al-Osta *et al*. 2021, Foroutan *et al*. 2022, Zerrouki *et al*. 2022). These thin, flat elements are widely used in aerospace, civil, and mechanical engineering applications, including bridges, buildings, ship hulls, and aircraft wings (Biglari and Jafari 2010). Their strength, stiffness, and lightweight nature make them crucial for designing durable and efficient structures (Viola *et al*. 2013). Engineers analyze plate behavior under various loading conditions, including bending, buckling, and vibration, to ensure safety and performance (Sheng *et al*. 2023). Advances in material science and computational modeling further enhance the design and optimization of plate structures for modern engineering challenges (Zhao *et al*. 2024).

Fig. 1 illustrates a smart sports flooring system equipped with an intelligent vibration controller designed to manage and mitigate structural vibrations induced by external excitations (https://engineeringsport.co.uk/). The system comprises a modular sports floor integrated with sensors and actuators, all housed within a structural aluminum truss framework. A projection unit mounted above the setup displays system feedback, likely linked to real-time data acquisition and control interfaces seen at the monitoring station. The core objective of this setup is to investigate the dynamic response of the flooring structure and regulate its vibrational behavior using adaptive control strategies. Such a system is essential for enhancing performance and safety in athletic environments by reducing excessive floor oscillations during gameplay. The intelligent vibration controller enables the system to adjust in real time, providing effective damping and ensuring structural stability. This experimental platform offers valuable insight into active vibration control methodologies applicable to advanced civil and sports engineering infrastructures.

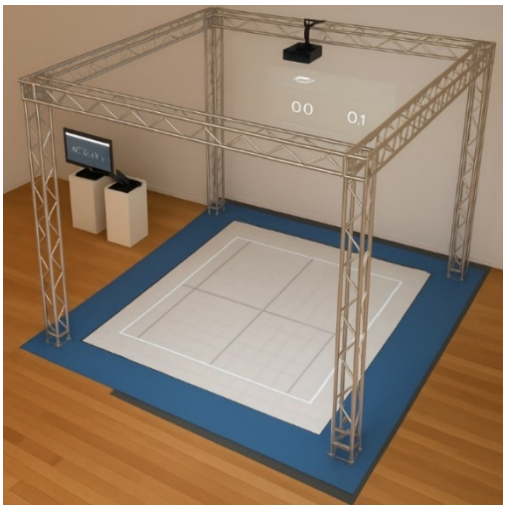

Fig. 1 A smart sports flooring system equipped with an intelligent vibration controller designed to manage and mitigate structural vibrations induced by external excitations

Machine learning algorithms are increasingly important for engineers as they enable data-driven decision-making, automation, and predictive modeling (Samaniego *et al*. 2020). These algorithms enhance engineering processes by identifying patterns, optimizing system performance, and improving efficiency in complex applications (Zhuang *et al*. 2021). Engineers apply machine learning in various fields, including robotics, manufacturing, structural analysis, and autonomous systems, to develop intelligent and adaptive solutions (Guo *et al*. 2021). The integration of advanced techniques such as deep learning and reinforcement learning allows for real-time monitoring, fault detection, and predictive maintenance (Mortazavi *et al*. 2025). As industries embrace digital transformation, machine learning algorithms play a vital role in advancing engineering innovation and problem-solving (Mortazavi *et al*. 2024).

For the first time, this research introduces a novel approach to vibration control in smart hybrid nanocomposite-reinforced sport structures, focusing on the TDF controller with DA as the primary control strategy. Utilizing the CUF, a comprehensive mathematical model is developed to capture the dynamic behavior of these structures under impact and oscillatory forces typical in sports applications. The TDF controller with DA is designed to enhance the system's ability to adapt to external disturbances by incorporating a time-delay mechanism, which optimally adjusts damping properties and improves stability without requiring complex real-time measurements. The hybrid nanocomposite material used—composed of ZnO, and GO—provides significant enhancements to the mechanical and electromechanical properties of the sport structures. Functionally graded nanocomposite face sheets, integrated with piezoelectric sensor-actuator layers, create an adaptive control environment that dynamically adjusts the damping properties of the structure, thus mitigating unwanted vibrations and ensuring stability during dynamic loading conditions. Through detailed simulations and performance analysis, the TDF controller with DA has been shown to outperform traditional control strategies by effectively reducing vibrations and improving dynamic stability. The approach demonstrated here holds significant promise for a wide range of sport structures, from high-performance sports equipment to large-scale infrastructure such as stadiums, where vibration control is crucial for both safety and performance. This research establishes a foundation for

developing next-generation adaptive sport structures that are both resilient and long-lasting under dynamic conditions. By integrating advanced material technologies and intelligent control strategies, the proposed solution offers a highly effective means of vibration suppression and stability enhancement, marking a significant step forward in sports engineering applications.

2. Mathematical modeling

A conceptual diagram in Fig. 2 presents a rectangular plate composed of ZnO (zinc oxide), and GO (graphene oxide) material, experiencing a force $F(t)$ that varies over time. The plate is positioned within a 3D coordinate framework $(\mathfrak{x}, \mathfrak{y}, \mathfrak{z})$, where the $\mathfrak{x}$ and $\mathfrak{y}$ axes define its surface, while the $\mathfrak{z}$-axis extends perpendicularly. This illustration likely supports research focused on the plate's vibrational behavior or dynamic response under varying load conditions.

2.1 Hybrid nanocomposite reinforcement

In this work, a hybrid nanocomposite reinforcement is used to improve the material properties of the core. It should be note that the abbreviation $ZnO—GO$ used in the equations is replaced with ϱ parameter.

2.1.1 Volume fraction of ZnO–GO reinforcement

The composite reinforcement's distribution pattern is mathematically defined by the following expressions.

Pattern 1 (Linear Distribution):

$$V_\varrho(k) = 4\left(\frac{|\mathfrak{z}_k|}{h^c}\right) V_\varrho^T, \tag{1}$$

Pattern 2 (Quadratic Distribution):

$$V_\varrho(k) = \left(2 - 4\left(\frac{|\mathfrak{z}_k|}{h^c}\right)\right) V_\varrho^T, \tag{2}$$

Pattern 3 (Uniform Distribution):

$$V_\varrho(k) = V_\varrho^T. \tag{3}$$

where $\mathfrak{z}_k = -\frac{h^c}{2} + \frac{k-1}{N_L-1} h^c,\ k = 1, \ldots, N_L, h^c$ is the total thickness core, and V_ϱ^T is the total reinforcement volume fraction.

2.1.2 Volume fraction based on density

$$V_\varrho^T = \frac{1}{1 + (\frac{\rho_\varrho}{\rho_M})(\frac{1}{W_{ncm}} - 1)}. \tag{4}$$

Where W_{ncm} is the weight fraction, and ρ denotes density.

2.1.3 Effective Young's Modulus (Halpin-Tsai Model)

The effective Young's modulus of the nanocomposite, can be predicted by the Halpin-Tsai model

$$E^{(k)}(z) = 0.49E_l + 0.51E_t, \tag{5}$$

Where longitudinal and transverse moduli are computed as

$$E_l = \frac{E_M(1 + \xi_l \eta_l V_\varrho)}{1 - \eta_l V_\varrho}, \qquad E_t = \frac{E_M(1 + \xi_t \eta_t V_\varrho)}{1 - \eta_t V_\varrho}. \tag{6}$$

where

$$\eta_l = \frac{\left(\frac{E_\varrho}{E_M}\right) - 1}{\left(\frac{E_\varrho}{E_M}\right) + \xi_l}, \qquad \eta_t = \frac{\left(\frac{E_\varrho}{E_M}\right) - 1}{\left(\frac{E_\varrho}{E_M}\right) + \xi_t}. \tag{7}$$

where E_ϱ is the elastic modulus of the reinforcement, and ξ_l, ξ_t are geometry factors.

2.1.4 Geometry factor

ξ_l and ξ_t are the parameters characterizing both the geometry and size of naofillers, defined as

$$\xi_l = \xi_t = \frac{2d_\varrho}{h_\varrho}. \tag{8}$$

where d_ϱ and h_ϱ are the diameter and thickness of the reinforcement phase.

2.1.5. Poisson's Ratio

According to the rule of mixture, the effective Possion's ratio of the core can be calculated by way of

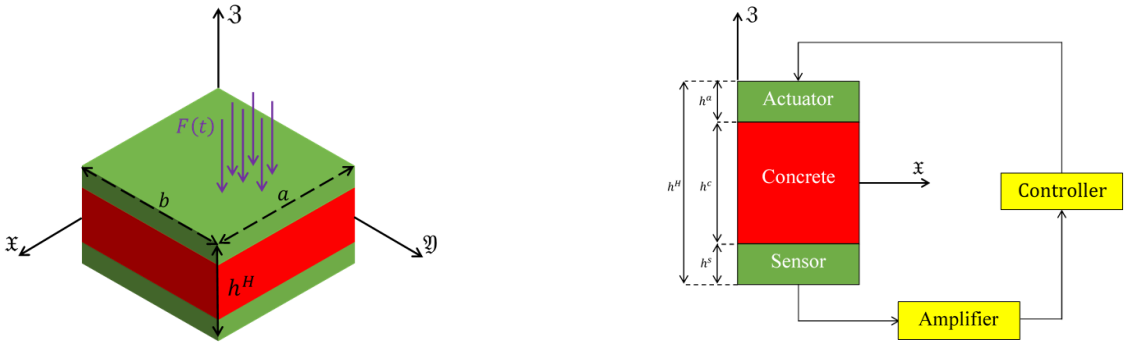

Fig. 2 A genuine schematic representation and geometry of the composite plate under external load

Table 1 Material properties of ϱ reinforcement and epoxy

Material	Elastic modulus (GPa)	Mass density (g/cm³)	Poisson's ratio (ν)
ZnO	140	5.6	0.34
GO	210	1.8	0.16
Epoxy matrix	25	2.3	0.2

$$\nu^{(k)}(z) = \nu_M V_M + \nu_\varrho V_\varrho. \tag{9}$$

Where ν_M and ν_ϱ are the Poisson's ratios of the matrix and reinforcement.

2.1.6 Mass density

According to the rule of mixture, the effective density of the core can be calculated by way of

$$\rho^{(k)}(z) = \rho_M V_M + \rho_\varrho V_\varrho. \tag{10}$$

This follows the same approach as Poisson's ratio.

2.1.7 Shear Modulus (Voigt-Reuss-Hill Model)

The effective shear modulus of the composite can be determined by the following equation.

$$G_{eff} = \frac{G_{upper} + G_{lower}}{2}, \tag{11}$$

where

$$\mathrm{G_{upper}} = \mathrm{V_M G_M} + \mathrm{V_\varrho}\, G_\varrho, \tag{12a}$$

$$G_{lower} = \left(\frac{V_M}{G_M} + \frac{\mathrm{V_\varrho}}{G_\varrho}\right)^{-1}. \tag{12b}$$

Table 1 provides a comparative summary of the material properties of ϱ, highlighting their elastic modulus, mass density, and Poisson's ratio.

3. Unified formulation

According to the CUF (Carrera 2003), the displacement fields can be presented as follows

$$\begin{aligned} &\mathfrak{U}^k(\mathfrak{x},\mathfrak{y},\mathfrak{Z}) = \mathfrak{H}_\tau(\mathfrak{Z})\mathfrak{U}^k_\tau(\mathfrak{x},\mathfrak{y}),\\ &\delta\mathfrak{U}^k(\mathfrak{x},\mathfrak{y},\mathfrak{Z}) = \mathfrak{H}_s(\mathfrak{Z})\delta\mathfrak{U}^k_s(\mathfrak{x},\mathfrak{y}),\\ &\Phi^k(\mathfrak{x},\mathfrak{y},\mathfrak{Z}) = \mathfrak{H}_\tau(\mathfrak{Z})\Phi^k_\tau(\mathfrak{x},\mathfrak{y}),\\ &\delta\Phi^k(\mathfrak{x},\mathfrak{y},\mathfrak{Z}) = \mathfrak{H}_s(\mathfrak{Z})\delta\Phi^k_s(\mathfrak{x},\mathfrak{y}), \end{aligned} \tag{13}$$

where

$$\begin{aligned} &\mathfrak{U} = \mathfrak{H}_0\mathfrak{U}_0 + \mathfrak{H}_1\mathfrak{U}_1 + \cdots + \mathfrak{H}_N\mathfrak{U}_N = \mathfrak{H}_s\mathfrak{U}_s,\\ &s = 0,1,\dots,N\\ &\mathfrak{H}_0 = \mathfrak{Z}^0 = 1, \quad \mathfrak{H}_1 = \mathfrak{Z}^1 = \mathfrak{Z},\dots,\mathfrak{H}_N = \mathfrak{Z}^N \end{aligned} \tag{14}$$

Classical approaches such as the first-order shear deformation theory (FSDT) can be obtained from an Equivalent Single Layer (ESL) model by setting $(N = 1)$ and applying penalty techniques to ensure the same transverse displacement throughout the thickness. To address Poisson's locking, a correction is applied to both the FSDT and the $(N = 1)$ ESL models, in line with earlier research (Carrera and Brischetto 2008). In contrast, Layerwise (LW) models define both displacement and potential for each individual layer.

$$\begin{aligned} &\mathfrak{U}^k = \mathfrak{H}_t\mathfrak{U}^k_t + \mathfrak{H}_b\mathfrak{U}^k_b + \mathfrak{H}_r\mathfrak{U}^k_r = \mathfrak{H}_\tau\mathfrak{U}^k_\tau,\\ &\quad \tau = t,b,r, \quad r = 2,\dots,N,\\ &\Phi^k = \mathfrak{H}_t\Phi^k_t + \mathfrak{H}_b\Phi^k_b + \mathfrak{H}_r\Phi^k_r = \mathfrak{H}_\tau\Phi^k_\tau,\\ &\quad \tau = t,b,r, \quad r = 2,\dots,N,\\ &\mathfrak{H}_t = \frac{\mathcal{P}_0 + \mathcal{P}_1}{2}, \quad \mathfrak{H}_b = \frac{\mathcal{P}_0 - \mathcal{P}_1}{2}, \quad \mathfrak{H}_r = \mathcal{P}_r - \mathcal{P}_{r-2}. \end{aligned} \tag{15}$$

in which $\mathcal{P}_j = \mathcal{P}_j(\zeta_k)$ is the Legendre polynomial of j-order defined in the ζ_k-domain: $\mathcal{P}_0 = 1, \mathcal{P}_1 = \zeta_k, \mathcal{P}_2 = (3\zeta_k^2 - 1)/2, \mathcal{P}_3 = (5\zeta_k^3 - 3\zeta_k)/2, \mathcal{P}_4 = (35\zeta_k^4 - 30\zeta_k^2 + 3)/8$. The values of displacement and potential at the top (t) and bottom (b) surfaces are considered as variables to be determined, with the following compatibility conditions imposed

$$\mathfrak{U}^k_t = \mathfrak{U}^{k+1}_b, \quad \Phi^k_t = \Phi^{k+1}_b, \qquad k = 1, \quad n_1 - 1 \tag{16}$$

In contrast to ESL models, Layerwise (LW) models can capture the zigzag variation of variables across the layers of a structure.

3.1 Plate geometry

This part describes the creation of a finite element (FE) designed for studying multilayered structures. The element is based on both Layerwise (LW) and Equivalent Single Layer (ESL) approaches within a Unified formulation framework. A nine-node plate element is adopted for the analysis. Plates are considered two-dimensional elements, characterized by a thickness (in the $\mathfrak{Z}$-direction) that is significantly smaller than their in-plane dimensions. In this work, the layer parameter (n_1) is assigned two values: ($n_1 = 1$) for the general plate, and ($n_1 = 3$) for areas containing embedded sensors and/or actuators. Fig. 2 illustrates the geometry and coordinate system. The relationships describing the geometry are presented in matrix notation below

$$\begin{aligned} \boldsymbol{\sigma}_p &= \left[\sigma_{\mathfrak{x}\mathfrak{x}}, \sigma_{\mathfrak{y}\mathfrak{y}}, \sigma_{\mathfrak{x}\mathfrak{y}}\right] = \left(\mathfrak{D}_p\right)\mathfrak{U},\\ \boldsymbol{\sigma}_n &= \left[\sigma_{\mathfrak{x}\mathfrak{Z}}, \sigma_{\mathfrak{y}\mathfrak{Z}}, \sigma_{\mathfrak{Z}\mathfrak{Z}}\right] = \left(\mathfrak{D}_{np} + \mathfrak{D}_{n\mathfrak{Z}}\right)\mathfrak{U}. \end{aligned} \tag{17}$$

where

$$\begin{aligned} &\mathfrak{D}_p = \begin{bmatrix} \partial_\mathfrak{x} & 0 & 0\\ 0 & \partial_\mathfrak{y} & 0\\ \partial_\mathfrak{y} & \partial_\mathfrak{x} & 0 \end{bmatrix}, \quad \mathfrak{D}_{np} = \begin{bmatrix} 0 & 0 & \partial_\mathfrak{x}\\ 0 & 0 & \partial_\mathfrak{y}\\ 0 & 0 & 0 \end{bmatrix},\\ &\mathfrak{D}_{n\mathfrak{Z}} = \begin{bmatrix} \partial_\mathfrak{Z} & 0 & 0\\ 0 & \partial_\mathfrak{Z} & 0\\ 0 & 0 & \partial_\mathfrak{Z} \end{bmatrix}. \end{aligned} \tag{18}$$

Also, we have

$$\begin{aligned} \mathrm{E}_p &= \left[\mathrm{E}_\mathfrak{x}, \mathrm{E}_\mathfrak{y}\right]^T = -\mathfrak{D}_{ep}\Phi,\\ \mathrm{E}_n &= \left[\mathrm{E}_\mathfrak{Z}\right]^T = -\mathfrak{D}_{en}\Phi. \end{aligned} \tag{19}$$

For differential operators have

$$\mathfrak{D}_{ep} = \begin{bmatrix} \partial_{\mathfrak{x}} \\ \partial_{\mathfrak{y}} \end{bmatrix}, \qquad \mathfrak{D}_{en} = \begin{bmatrix} \partial_{\mathfrak{Z}} \end{bmatrix} \tag{20}$$

4. Finite-element approximation and MITC method

Within the finite element approach, Lagrangian shape functions ($\mathfrak{N}_i$) are employed to interpolate the displacement and potential values at each node of the element

$$\begin{aligned} &\delta\mathfrak{U}_s = \mathfrak{N}_i \delta\mathbf{q}_{\mathcal{U}s_i}, \quad \mathfrak{U}_\tau = \mathfrak{N}_j \mathbf{q}_{\mathcal{U}\tau_j}, \\ &\quad \text{with} \quad i,j = 1,\dots,9 \\ &\delta\Phi_s = \mathfrak{N}_i \delta \mathrm{q}_{\Phi s_i}, \quad \Phi_\tau = \mathfrak{N}_j \mathrm{q}_{\Phi\tau_j} \\ &\quad \text{with} \quad i,j = 1,\dots,9 \end{aligned} \tag{21}$$

Additionally, let $\mathbf{q}_{\mathcal{U}\tau_j} = \left(\mathbf{q}_{\mathcal{U}_\tau}, \mathbf{q}_{\mathcal{V}_t}, \mathbf{q}_{\mathcal{W}_t}\right)$ represent the nodal electric potential and $\delta\mathbf{q}_{\mathcal{U}_s} = \left(\delta\mathbf{q}_{\mathcal{U}_s}, \delta\mathbf{q}_{\mathcal{V}_s}, \delta\mathbf{q}_{\mathcal{W}_s}\right)$ denote its virtual variation. By inserting these expressions into the geometric equations, we arrive at

$$\begin{aligned} &\boldsymbol{\mathcal{E}}_p = \mathfrak{H}_\tau\left(\mathfrak{D}_p\right)(\mathfrak{N}_i)\mathbf{q}_{\tau_i}, \\ &\boldsymbol{\mathcal{E}}_n = \mathfrak{H}_\tau(\mathfrak{D}_{n\Omega})(\mathfrak{N}_i)\mathbf{q}_{\tau_i} + \mathfrak{H}_{\tau,\mathfrak{Z}}\mathfrak{D}_{n\mathfrak{Z}}(\mathfrak{N}_i)\mathbf{q}_{\tau_i}. \end{aligned} \tag{22}$$

In the local coordinate system (ξ, η), the MITC plate elements (Bathe and Dvorkin 1986, Bucalem and Bathe 1993) are formulated by interpolating strain components within each element, rather than calculating them solely from displacement fields. The corresponding interpolation functions for these strains are organized in the arrays below

$$\begin{aligned} &\boldsymbol{\mathcal{N}}_{m1} = \left[\mathfrak{N}_{\mathfrak{A}1}, \mathfrak{N}_{\mathfrak{B}1}, \mathfrak{N}_{\mathfrak{C}1}, \mathfrak{N}_{\mathfrak{D}1}, \mathfrak{N}_{\mathfrak{F}1}, \mathfrak{N}_{\mathfrak{H}1}\right], \\ &\boldsymbol{\mathcal{N}}_{m3} = \left[\mathfrak{N}_P, \mathfrak{N}_Q, \mathfrak{N}_R, \mathfrak{N}_S\right]. \end{aligned} \tag{23}$$

From this point onward, the subscripts $m1, m2$, and $m3$ represent quantities computed at the points $(\mathfrak{A}1, \mathfrak{B}1, \mathfrak{C}1, \mathfrak{D}1, \mathfrak{F}1, \mathfrak{H}1)$, $(\mathfrak{A}2, \mathfrak{B}2, \mathfrak{C}2, \mathfrak{D}2, \mathfrak{F}2, \mathfrak{H}2)$ and (P, Q, R, S), respectively. Consequently, the strain components can be formulated as

$$\begin{aligned} \boldsymbol{\mathcal{E}}_{\mathrm{p}} &= \begin{bmatrix} \epsilon_{\mathfrak{x}\mathfrak{x}} \\ \epsilon_{\mathfrak{y}\mathfrak{y}} \\ \gamma_{\mathfrak{x}\mathfrak{y}} \end{bmatrix} = \begin{bmatrix} \mathfrak{N}_{\mathrm{m1}} & 0 & 0 \\ 0 & \mathfrak{N}_{\mathrm{m2}} & 0 \\ 0 & 0 & \mathfrak{N}_{\mathrm{m3}} \end{bmatrix} \begin{bmatrix} \epsilon_{\mathfrak{x}\mathfrak{x}_{\mathrm{m1}}} \\ \epsilon_{\mathfrak{y}\mathfrak{y}_{\mathrm{m2}}} \\ \gamma_{\mathfrak{x}\mathfrak{y}_{\mathrm{m3}}} \end{bmatrix}, \\ \boldsymbol{\mathcal{E}}_{\mathrm{n}} &= \begin{bmatrix} \gamma_{\mathfrak{x}\mathfrak{Z}} \\ \gamma_{\mathfrak{y}\mathfrak{Z}} \\ \epsilon_{\mathfrak{Z}\mathfrak{Z}} \end{bmatrix} = \begin{bmatrix} \mathfrak{N}_{\mathrm{m1}} & 0 & 0 \\ 0 & \mathfrak{N}_{\mathrm{m2}} & 0 \\ 0 & 0 & 1 \end{bmatrix} \begin{bmatrix} \gamma_{\mathfrak{x}\mathfrak{Z}_{\mathrm{m1}}} \\ \gamma_{\mathfrak{y}\mathfrak{Z}_{\mathrm{m2}}} \\ \epsilon_{\mathfrak{Z}\mathfrak{Z}} \end{bmatrix}. \end{aligned} \tag{24}$$

The strain components $\epsilon_{\mathfrak{x}\mathfrak{x}_{m1}}$, $\epsilon_{\mathfrak{y}\mathfrak{y}_{m2}}$, $\epsilon_{\mathfrak{x}\mathfrak{y}_{m3}}$, $\epsilon_{\mathfrak{x}\mathfrak{Z}_{m1}}$, $\epsilon_{\mathfrak{y}\mathfrak{Z}_{m2}}$ are determined using Eq. (22), with the shape functions $\mathfrak{N}_i$ evaluated at the tying points.

5. Constitutive equations

The next step in deriving the governing equations involves defining constitutive models that connect stress and electric displacement to strain and electric field variables. To achieve this, a linear constitutive approach is employed, utilizing the generalized Hooke's law applicable for small deformations. This framework also features a linear interaction between mechanical and electrical behaviors, allowing for the influence of electric fields to be incorporated. While the presented numerical analysis focuses on isotropic plates with embedded piezoelectric elements, the constitutive models are broadly formulated to permit the analysis of composite structures in future research. Initially, these relationships are expressed in the local material axes (1,2,3) for each individual layer (k), and subsequently converted into the global coordinate system $(\mathfrak{X}, \mathfrak{Y}, \mathfrak{Z})$. Consequently, the transformed stress components $\boldsymbol{\sigma}_p^k = \left\{\sigma_{\mathfrak{x}\mathfrak{x}}^k, \sigma_{\mathfrak{y}\mathfrak{y}}^k, \sigma_{\mathfrak{x}\mathfrak{y}}^k\right\}$ and $\boldsymbol{\sigma}_n^k = \left\{\sigma_{\mathfrak{x}\mathfrak{Z}}^k, \sigma_{\mathfrak{y}\mathfrak{Z}}^k, \sigma_{\mathfrak{Z}\mathfrak{Z}}^k\right\}$, as well as the electric displacement vectors $\left(\mathfrak{D}_p^k = \left\{\mathcal{D}_{\mathfrak{x}}^k, \mathcal{D}_{\mathfrak{y}}^k\right\}\right.$ and $\left.\mathfrak{D}_n^k = \left\{\mathcal{D}_{\mathfrak{Z}}^k\right\}\right)$, can be represented as follows

$$\begin{aligned} \boldsymbol{\sigma}_{p\mathfrak{C}}^k &= \mathfrak{c}_{pp}^k \mathcal{E}_{pG}^k + \mathfrak{c}_{pn}^k \mathcal{E}_{nG}^k - \boldsymbol{e}_{pp}^{k^T} \mathbf{E}_{pG}^k - \boldsymbol{e}_{np}^{k^T \mathbf{E}_{nG}^k}, \\ \boldsymbol{\sigma}_{n\mathfrak{C}}^k &= \mathfrak{c}_{np}^k \mathcal{E}_{pG}^k + \mathfrak{c}_{nn}^k \mathcal{E}_{nG}^k - \boldsymbol{e}_{pn}^{k^T} \mathbf{E}_{pG}^k - \boldsymbol{e}_{nn}^{k^T} \mathbf{E}_{nG}^k, \\ \mathfrak{D}_{p\mathfrak{C}}^k &= \boldsymbol{e}_{pp}^k \mathcal{E}_{pG}^k + \boldsymbol{e}_{pn}^k \mathcal{E}_{nG}^k + \boldsymbol{\varepsilon}_{pp}^k \mathbf{E}_{pG}^k + \boldsymbol{\varepsilon}_{pn}^k \mathbf{E}_{nG}^k, \\ \mathfrak{D}_{n\mathfrak{C}}^k &= \boldsymbol{e}_{np}^k \mathcal{E}_{pG}^k + e_{nn}^k \mathcal{E}_{nG}^k + \boldsymbol{\varepsilon}_{np}^k \mathbf{E}_{pG}^k + \boldsymbol{\varepsilon}_{nn}^k \mathbf{E}_{nG}^k. \end{aligned} \tag{25}$$

where

$$\begin{aligned} \mathfrak{c}_{pp}^k &= \begin{bmatrix} \mathfrak{C}_{11}^k & \mathfrak{C}_{12}^k & 0 \\ \mathfrak{C}_{12}^k & \mathfrak{C}_{22}^k & 0 \\ 0 & 0 & \mathfrak{C}_{66}^k \end{bmatrix}, \quad \mathfrak{c}_{pn}^k = \begin{bmatrix} 0 & 0 & \mathfrak{C}_{13}^k \\ 0 & 0 & \mathfrak{C}_{23}^k \\ 0 & 0 & 0 \end{bmatrix}, \\ \mathfrak{c}_{np}^k &= \begin{bmatrix} 0 & 0 & 0 \\ 0 & 0 & 0 \\ \mathfrak{C}_{13}^k & \mathfrak{C}_{23}^k & 0 \end{bmatrix}, \quad \mathfrak{c}_{nn}^k = \begin{bmatrix} \mathfrak{C}_{55}^k & 0 & 0 \\ 0 & \mathfrak{C}_{44}^k & 0 \\ 0 & 0 & \mathfrak{C}_{33}^k \end{bmatrix}, \\ \boldsymbol{e}_{pp}^k &= \begin{bmatrix} 0 & 0 & 0 \\ 0 & 0 & 0 \end{bmatrix}, \quad \boldsymbol{e}_{pn}^k = \begin{bmatrix} e_{15}^k & e_{14}^k & 0 \\ e_{25}^k & e_{24}^k & 0 \end{bmatrix}, \\ \boldsymbol{e}_{np}^k &= \begin{bmatrix} e_{31}^k & e_{32}^k & e_{36}^k \end{bmatrix}, \quad \boldsymbol{e}_{nn}^k = \begin{bmatrix} 0 & 0 & e_{33}^k \end{bmatrix} \\ \boldsymbol{\varepsilon}_{pp}^k &= \begin{bmatrix} \varepsilon_{11}^k & \varepsilon_{12}^k \\ \varepsilon_{12}^k & \varepsilon_{22}^k \end{bmatrix}, \quad \boldsymbol{\varepsilon}_{pn}^k = \begin{bmatrix} 0 \\ 0 \end{bmatrix}, \\ \boldsymbol{\varepsilon}_{np}^k &= \begin{bmatrix} 0 & 0 \end{bmatrix}, \quad \boldsymbol{\varepsilon}_{nn}^k = \begin{bmatrix} \varepsilon_{33}^k \end{bmatrix} \end{aligned} \tag{26}$$

Also, have (Reddy 2003)

$$\begin{aligned} &\mathfrak{C}_{11}^k = \frac{\mathfrak{F}^{(k)}\left(1 - \nu^{(k)}\right)}{(1 + \nu^{(k)})(1 - 2\nu^{(k)})}, \\ &\mathfrak{C}_{12}^k = \frac{\mathfrak{F}^{(k)}\nu^{(k)}}{(1 + \nu^{(k)})(1 - 2\nu^{(k)})}, \\ &\mathfrak{C}_{33}^k = \mathfrak{C}_{22}^k = \mathfrak{C}_{11}^k, \\ &\mathfrak{C}_{13}^k = \mathfrak{C}_{23}^k = \mathfrak{C}_{12}^k, \mathfrak{C}_{44}^k = \mathfrak{C}_{55}^k = \mathfrak{C}_{66}^k = G_{eff}, \\ &e_{15}^k = e_{14}^k = e_{25}^k = e_{24}^k = e_{31}^k = e_{32}^k = e_{36}^k = e_{33}^k = 0, \\ &\varepsilon_{11}^k = \varepsilon_{12}^k = \varepsilon_{22}^k = \varepsilon_{33}^k = 0. \end{aligned} \tag{27}$$

where (Wang *et al*. 2024)

$$\begin{aligned} &\mathfrak{C}_{11}^k = \frac{\mathfrak{F}_{11}}{\Delta}(1 - \nu_{23}\nu_{32}), \quad \mathfrak{C}_{22}^k = \frac{\mathfrak{F}_{22}}{\Delta}(1 - \nu_{31}\nu_{13}), \\ &\mathfrak{C}_{33}^k = \frac{\mathfrak{F}_{33}}{\Delta}(1 - \nu_{12}\nu_{21}), \quad \mathfrak{C}_{44}^k = G_{23}, \\ &\mathfrak{C}_{55}^k = G_{13}, \quad \mathfrak{C}_{66}^k = G_{12} \\ &\mathfrak{C}_{12}^k = \frac{\mathfrak{F}_{11}}{\Delta}(\nu_{21} + \nu_{31}\nu_{23}), \quad \mathfrak{C}_{13}^k = \frac{\mathfrak{F}_{11}}{\Delta}(\nu_{31} + \nu_{21}\nu_{32}), \\ &\mathfrak{C}_{23}^k = \frac{\mathfrak{F}_{22}}{\Delta}(\nu_{32} + \nu_{12}\nu_{31}), \\ &\Delta = 1 - \nu_{12}\nu_{21} - \nu_{23}\nu_{32} - \nu_{31}\nu_{13} - 2\nu_{12}\nu_{32}\nu_{13}. \end{aligned} \tag{28}$$

The properties of the piezoelectric layer are given in Ref. (Kumar and Harsha 2021). The piezoelectric material is characterized by its stiffness coefficients and its permittivity coefficients. Within the scope of this study, the stiffness coefficients are obtained from the piezoelectric coefficients according to the following expression

$$\mathbf{e}^{k^T} = \mathbf{C}^k \mathbf{d}^{k^T}. \tag{29}$$

where

$$\begin{aligned} \boldsymbol{d}_{pp}^k &= \begin{bmatrix} 0 & 0 & 0 \\ 0 & 0 & 0 \end{bmatrix}, \qquad \boldsymbol{d}_{pn}^k = \begin{bmatrix} d_{15}^k & d_{14}^k & 0 \\ d_{25}^k & d_{24}^k & 0 \end{bmatrix}. \\ \boldsymbol{d}_{np}^k &= [d_{31}^k \quad d_{32}^k \quad d_{36}^k], \quad \boldsymbol{d}_{nn}^k = [0 \quad 0 \quad d_{33}^k]. \end{aligned} \tag{30}$$

6. Governing equations and FE matrices

This part presents the development of the finite element stiffness matrix based on the Power Series Expansion (PVD) approach for multilayered plate systems under combined mechanical and electrical loading. The PVD representation for a multilayered piezoelectric assembly is formulated as

$$\int_V \left(\delta \boldsymbol{\mathcal{E}}_{pG}^T \boldsymbol{\sigma}_{p\mathbb{C}} + \delta \boldsymbol{\mathcal{E}}_{nG}^T \boldsymbol{\sigma}_{n\mathbb{C}} - \delta \mathbf{E}_{pG}^T \mathfrak{D}_{p\mathbb{C}} - \delta \mathbf{E}_{pG}^T \mathfrak{D}_{\mathrm{pC}}\right) dV = \delta L_{\mathrm{e}} - \delta L_{\mathrm{in}}. \tag{31}$$

In this context, denotes the volume and serves as the integration domain for the structure. The initial term in the equation accounts for the variation in internal work, whereas the following terms correspond to the external work and the inertial work, respectively. To ensure that the integration domains are consistent with the midsurface of each layer in the plate's coordinate system and the thickness direction, the integral notation below is introduced

$$\int_{\Omega_k} \int_{\mathfrak{A}_k} \left\{\delta \boldsymbol{\mathcal{E}}_{pG}^{k\ T} \boldsymbol{\sigma}_{p\mathbb{C}}^k + \delta \boldsymbol{\mathcal{E}}_{nG}^{k\ T} \boldsymbol{\sigma}_{n\mathbb{C}}^k - \delta \mathbf{E}_{pG}^{k\ T} \mathfrak{D}_{p\mathbb{C}}^k - \delta \mathbf{E}_{pG}^{k\ T} \mathfrak{D}_{p\mathbb{C}}^k\right\} d\Omega_k d\mathfrak{Z} = \delta L_{\mathrm{e}} - \delta L_{\mathrm{in}}. \tag{32}$$

where

$$\delta L_{\mathrm{in}} = \int_{\Omega_k} \int_{\mathfrak{A}_k} \{\rho \delta \mathfrak{U}^T \ddot{\mathfrak{U}}\} d\Omega_k d\mathfrak{Z}. \tag{33}$$

where

$$\begin{aligned} \delta \mathfrak{U}_s^k &: \quad \mathfrak{K}_{\mathcal{U}\mathcal{U}}^{k\tau s} \mathfrak{U}_\tau^k + \mathfrak{K}_{\mathcal{U}\phi}^{k\tau s} \boldsymbol{\Phi}_\tau^k + \mathfrak{M}_{\mathcal{U}\mathcal{U}}^{k\tau s} \ddot{\mathfrak{U}}_\tau^k = \boldsymbol{P}_{\mathcal{U}s}^k, \\ \delta \boldsymbol{\Phi}_s^k &: \quad \mathfrak{K}_{\Phi\mathcal{U}}^{kss} \mathcal{U}_\tau^k + \mathfrak{K}_{\Phi\Phi}^{k\tau s} \boldsymbol{\Phi}_\tau^k = \boldsymbol{P}_{\Phi s}^k. \end{aligned} \tag{34}$$

In compact form

$$\delta \mathbf{q}_s^k : \quad \mathfrak{K}^{kts} \mathbf{q}_\tau^k + \mathfrak{M}^{k\tau s} \ddot{\mathbf{q}}_\tau^k = \boldsymbol{P}_s^k. \tag{35}$$

where

$$\begin{aligned} \mathfrak{K}^{kts} &= \begin{bmatrix} \mathfrak{K}_{\mathcal{U}\mathcal{U}} & \mathfrak{K}_{\mathcal{U}\Phi} \\ \mathfrak{K}_{\Phi\mathcal{U}} & \mathfrak{K}_{\Phi\Phi} \end{bmatrix}^{kts}, \quad \mathfrak{M}^{k\tau s} = \begin{bmatrix} \mathfrak{M}_{\mathcal{U}\mathcal{U}} & 0 \\ 0 & 0 \end{bmatrix}^{k\tau s}, \\ \boldsymbol{P}_s^k &= \begin{bmatrix} \boldsymbol{P}_{\mathcal{U}s}^k \\ \boldsymbol{P}_{\Phi s}^k \end{bmatrix}^{k\tau s}. \end{aligned} \tag{36}$$

The external mechanical load applied and the surface charge density on the actuator layer are denoted by $\mathrm{q}_{\mathcal{W}_t} = F(t) = P_0 \sin(\Omega_{ext} t)$ and $\mathrm{q}_{\Phi_t} = q^a$, respectively.

7. Controller scheme

The mathematical version of this kind of controller (Time-Delay Feedback Controller with Derivative Action (TDF controller with DA) is as follows

$$\Phi^a = -\mathbb{G}_{\mathrm{v}} \dot{\Phi}^s - \mathbb{G}_d |\Phi^s(t) - \Phi^s(t-\tau)|. \tag{37}$$

where

$\mathbb{G}_{\mathrm{v}}$ is velocity feedback gain,
$\mathbb{G}_d$ is delayed proportional gain,
τ is the time delay.

8. Solution procedure

The corresponding matrix formulation of this system is expressed as follows

$$\delta \mathbf{q}_s^k : \quad \mathfrak{K}^{kts} \mathbf{q}_\tau^k + \mathfrak{M}^{k\tau s} \ddot{\mathbf{q}}_\tau^k = \boldsymbol{P}_s^k. \tag{38}$$

In the provided equations, '$\mathfrak{M}^{k\tau s}$', ' $\mathfrak{K}^{kts}$' represent the mass, damping, and stiffness matrices, respectively. The vectors for the applied force and unknown variables are denoted by ' $\boldsymbol{P}_s^k$' and '$\mathbf{q}$'. The subsequent initial conditions delineate the plate's state prior to loading while it remains at rest.

$$\mathbf{q}_\tau^k(0) = 0, \qquad \dot{\mathbf{q}}_\tau^k = 0. \tag{39}$$

By applying the Laplace transform to Eq. (39), the dynamic response of the motion equations is derived, where s is the Laplace transform parameter introduced for simplicity. Under these circumstances, a new system of equations—free of time dependence—is obtained by transforming Eq. (38) and incorporating the initial conditions given in Eq. (39). For example, the governing equations for the active control scenario in the Laplace domain are formulated as follows

$$\left[\widehat{\mathfrak{K}}^{kts} + s^2 \widehat{\mathfrak{M}}^{k\tau s}\right] \{\hat{\mathbf{q}}_\tau^k\} = \left\{\widehat{\boldsymbol{P}}_s^k\right\}. \tag{40}$$

In this formulation, a bar placed over each quantity indicates its corresponding Laplace-transformed version. By solving the system in Eq. (40), the displacement vector components are obtained in a closed-form expression within the Laplace domain. To convert the displacement vector back to the time domain, the inverse Laplace transform is applied. For each layer, Eq. (40) is solved after the Laplace transform, providing the displacement components for that specific layer (Nguyen *et al*. 2022). To fully transition from the Laplace domain to the time domain, the modified Dubner and Abate method (Durbin 1974) is utilized, which

allows for the retrieval of time-dependent values such as displacements, stresses, heat flow, and temperature gradients.

9. Application of DNN algorithm to estimate vibration-control of the presented sandwich structure with piezoelectric face sheets

Recent advancements in smart materials and intelligent systems have accelerated the application of artificial intelligence in structural dynamics. In this context, DNNs have emerged as powerful tools for modeling complex relationships between mechanical responses and control inputs, particularly in structures embedded with piezoelectric components. This study presents a supervised DNN-based estimation framework to predict the vibration response of sandwich structures with piezoelectric face sheets under dynamic loading. These piezoelectric layers act as both sensors and actuators, converting mechanical strain into electrical signals and vice versa, making the system inherently suitable for active vibration control. The proposed DNN model takes as input the time history of displacement, velocity, and control voltage signals and outputs the predicted structural response. The architecture includes multiple fully connected layers with nonlinear activation functions such as ReLU or tanh, enabling the network to capture intricate electromechanical behaviors. The DNN is trained on a dataset generated either through finite element simulations or experimental measurements. Model performance is evaluated using key statistical and error metrics to ensure accurate and robust vibration estimation. The following formulations are adopted:

Mean squared error (MSE): Measures average squared differences between predicted and actual values

$$MSE = \frac{1}{N}\sum_{i=1}^{N}(y_i - \hat{y}_i)^2. \tag{41}$$

Root mean squared error (RMSE): Emphasizes larger errors, providing intuitive insight into prediction accuracy

$$RMSE = \sqrt{\frac{1}{N}\sum_{i=1}^{N}(y_i - \hat{y}_i)^2}. \tag{42}$$

Coefficient of determination (R^2): Indicates the proportion of variance explained by the model

$$R^2 = 1 - \frac{\sum_{i=1}^{N}(y_i - \hat{y}_i)^2}{\sum_{i=1}^{N}(y_i - \bar{y})^2}. \tag{43}$$

Mean absolute error (MAE): Represents the average absolute error between predictions and true values

$$MAE = \frac{1}{N}\sum_{i=1}^{N}|y_i - \hat{y}_i|. \tag{44}$$

Loss function for optimization: Based on MSE, used during training

Table 2 A comparison of the dimensionless central deflections of a square functionally graded plate subjected to a uniform load, with an aspect ratio of $a/h = 5$

Method	ϑ			
	0	**0.5**	**1**	**2**
CUF (Present)	0.1718	0.2319	0.2727	0.3198
Ref. (Lee *et al*. 2009)	0.1722	0.2403	0.2811	0.3221

$$L(\theta) = \frac{1}{N}\sum_{i=1}^{N}(y_i - F_{\mathfrak{D}NN}(x_i;\theta))^2. \tag{45}$$

Overall, the DNN provides a data-driven alternative for real-time vibration estimation, reducing reliance on complex physical modeling and enabling adaptive control strategies in smart composite systems.

10. Results and discussion

10.1 Verification study

Table 2 presents a comparison of the dimensionless central deflections for a square functionally graded plate under a uniform load, with an aspect ratio of $\mathrm{a/h} = 5$. The deflection values are provided for various material gradient indices, ranging from 0 to 2. The results obtained using the present method are compared with those from previous studies, including references (Nguyen-Xuan *et al*. 2011), (Gilhooley *et al*. 2007), and (Lee *et al*. 2009). For $\vartheta = 0$, the present study yields a central deflection of 0.1715, which is in close agreement with the values reported in the literature, ranging between 0.1671 and 0.1722. As the gradient index increases, all methods demonstrate an increasing trend in deflection, indicating that the stiffness of the functionally graded plate decreases with a higher proportion of softer material. For $\vartheta = 2$, the deflections range from 0.3118 (present) to 0.3280 (Ref. (Gilhooley *et al*. 2007)), showcasing slight variations due to differences in methodologies and numerical approaches. The consistency between the present method and prior studies validates the accuracy of the proposed formulation, as the deviations remain within an acceptable margin. This comparison highlights the reliability of the present approach in predicting the structural response of functionally graded plates under mechanical loading.

10.2 Parametric results

Fig. 3 evaluates the performance of three different nanocomposite spatial distributions—linear (Pattern 1), quadratic (Pattern 2), and uniform (Pattern 3)—when subjected to the Time-Delay Feedback (TDF) controller. Subplot (a) demonstrates that all three patterns achieve effective damping of vibrations, with Pattern 3 showing the quickest reduction in vibration amplitude. This suggests that a uniform nanocomposite distribution enhances the mechanical-electrical interaction, leading to better vibration

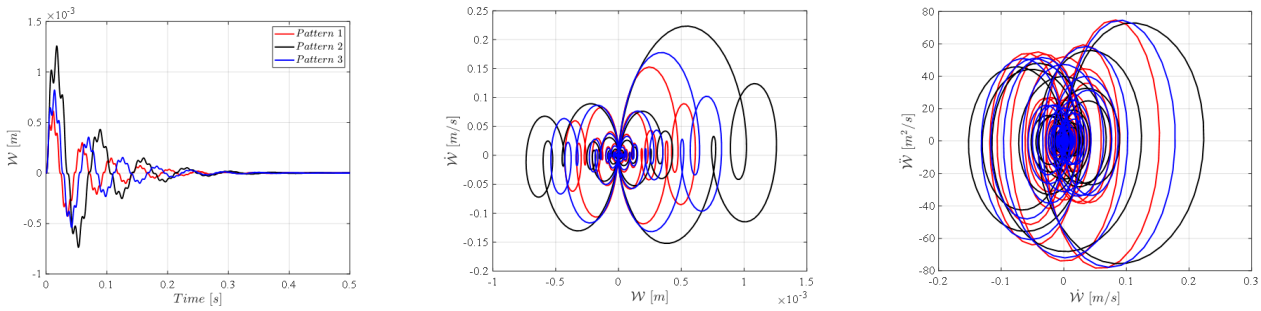

(a) $\mathcal{W}[m] - Time[s]$ (b) $\dot{\mathcal{W}}\left[\frac{m}{s}\right] - \mathcal{W}[m]$ (c) $\ddot{\mathcal{W}}\left[\frac{m^2}{s}\right] - \dot{\mathcal{W}}\left[\frac{m}{s}\right]$

Fig. 3 Three nanocomposite spatial distributions—linear (Pattern 1), quadratic (Pattern 2), and uniform (Pattern 3) —under the TDF controller

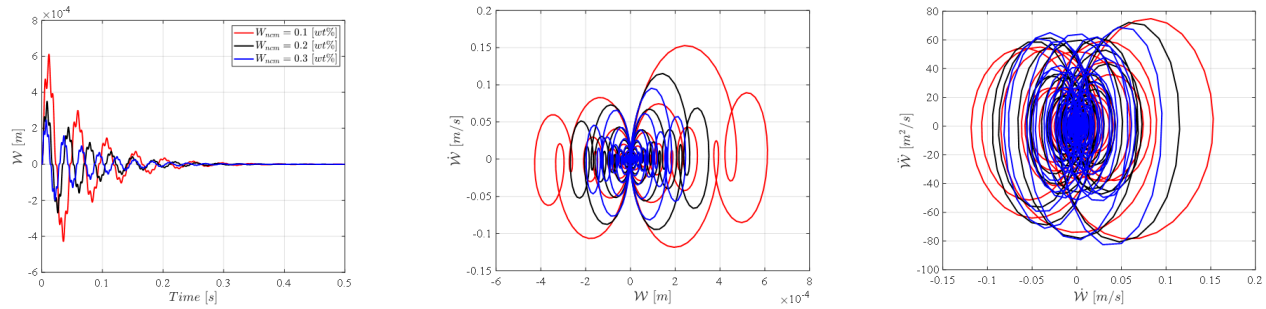

(a) $\mathcal{W}[m] - Time[s]$ (b) $\dot{\mathcal{W}}\left[\frac{m}{s}\right] - \mathcal{W}[m]$ (c) $\ddot{\mathcal{W}}\left[\frac{m^2}{s}\right] - \dot{\mathcal{W}}\left[\frac{m}{s}\right]$

Fig. 4 The influence of nanocomposite weight fractions under Pattern 1 (linear distribution) on the vibration control with with presented controller of the current smart system

control. Subplots (b) and (c) illustrate the phase space representations of the system's state variables ($\dot{\mathcal{W}} - \mathcal{W}$ and $\ddot{\mathcal{W}} - \dot{\mathcal{W}}$), where the denser trajectory core in Pattern 3 indicates superior dynamic response and stability. In contrast, Patterns 1 and 2 display broader oscillatory loops, signaling less efficient control. The results suggest that the homogeneity of Pattern 3, which evenly distributes the nanocomposite material, contributes to its superior performance when integrated with advanced control methods like the TDF controller. These findings highlight the adaptability of the CUF in optimizing smart flooring systems and reinforce the potential for enhancing real-world applications in dynamic environments requiring high-performance vibration control.

Fig. 4 investigates the impact of varying nanocomposite weight fractions ($W_{ncm} = 0.1, 0.2, 0.3\ wt\%$) under a linear distribution (Pattern 1) on vibration control with the presented controller. Subplot (a) reveals that higher weight fractions result in increased initial oscillations but faster decay of vibrations, particularly at 0.3 wt%, suggesting improved damping effects. This is attributed to the enhanced material stiffness and stronger piezoelectric coupling at higher nanocomposite concentrations. In subplots (b) and (c), the phase space representations ($\dot{\mathcal{W}} - \mathcal{W}$ and $\ddot{\mathcal{W}} - \dot{\mathcal{W}}$) show denser trajectory loops for higher W_{ncm}, confirming better energy dissipation and more effective vibration control. However, the higher initial peak amplitudes for larger weight fractions also indicate a trade-off with inertial effects, where more substantial material concentrations lead to a delayed initial response before achieving stabilization. These findings highlight the importance of fine-tuning nanocomposite weight fractions as part of the CUF to optimize performance, making it particularly suitable for smart sports flooring systems where precise vibration control is critical for long-term durability and effectiveness.

Fig. 5 investigates how increasing force amplitudes affect the vibration response of the system. Subfigure (a) presents time histories of transverse displacement under three levels of harmonic excitation: P_0, $2P_0$, and $3P_0$. The data show that the vibration response peaks quickly and stabilizes swiftly, demonstrating the effectiveness of the TDF controller with derivative action in mitigating oscillations, even under higher excitation levels. Subfigures (b) and (c) depict phase-plane portraits, with plots of $\dot{\mathcal{W}} - \mathcal{W}$ and $\ddot{\mathcal{W}} - \dot{\mathcal{W}}$, respectively. As the excitation increases, the loops in these plots broaden, indicating greater vibrational energy. However, despite the increase in excitation, the system eventually converges to a damped state, suggesting that the TDF-DA controller maintains stability and effectively dissipates energy over time. These results emphasize the robustness of the proposed control strategy, confirming its ability to handle varying dynamic loads and maintain control under different levels of

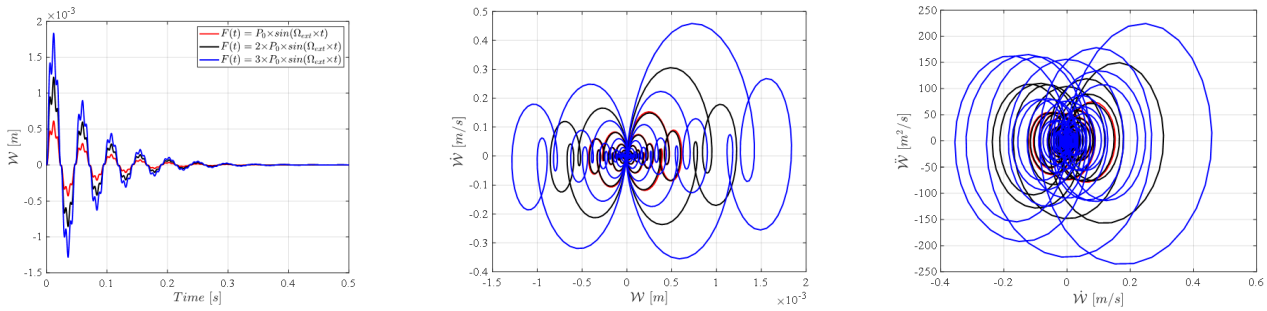

(a) $\mathcal{W}[m] - Time[s]$ (b) $\dot{\mathcal{W}}\left[\frac{m}{s}\right] - \mathcal{W}[m]$ (c) $\ddot{\mathcal{W}}\left[\frac{m^2}{s}\right] - \dot{\mathcal{W}}\left[\frac{m}{s}\right]$

Fig. 5 The effect of increasing force amplitudes on vibration response considering with presented controller, and pattern 1 of nanocomposite reinforcement

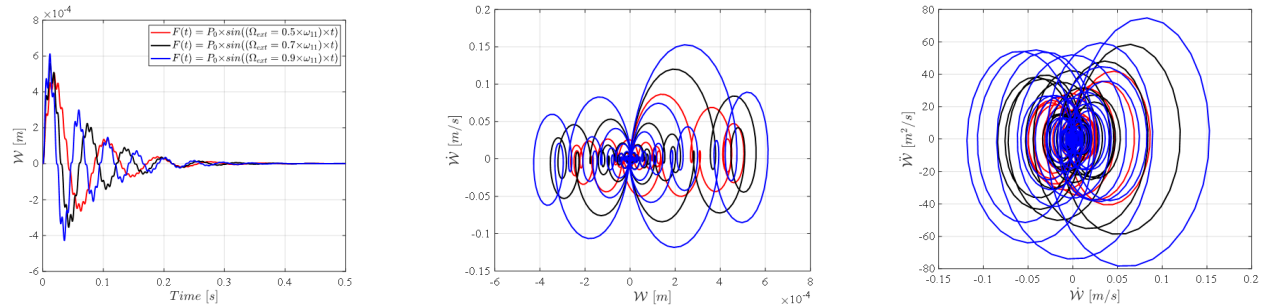

(a) $\mathcal{W}[m] - Time[s]$ (b) $\dot{\mathcal{W}}\left[\frac{m}{s}\right] - \mathcal{W}[m]$ (c) $\ddot{\mathcal{W}}\left[\frac{m^2}{s}\right] - \dot{\mathcal{W}}\left[\frac{m}{s}\right]$

Fig. 6 The sensitivity of the system to excitation frequency near the first natural frequency considering with presented controller, and Pattern 1 of nanocomposite reinforcement

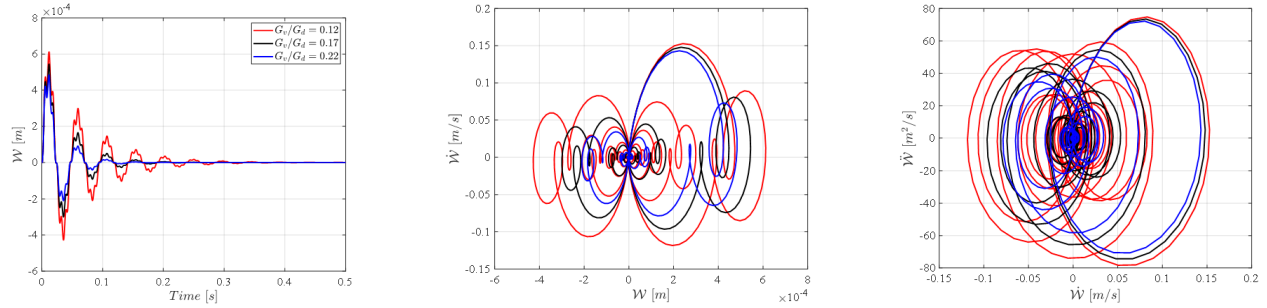

(a) $\mathcal{W}[m] - Time[s]$ (b) $\dot{\mathcal{W}}\left[\frac{m}{s}\right] - \mathcal{W}[m]$ (c) $\ddot{\mathcal{W}}\left[\frac{m^2}{s}\right] - \dot{\mathcal{W}}\left[\frac{m}{s}\right]$

Fig. 7 The influence of the control parameter $\mathbb{G}_v/\mathbb{G}_d$, governing the balance between velocity and displacement feedback considering $F(t) = P_0\, sin(\Omega_{ext} t)$, with presented controller, and Pattern 1 of nanocomposite reinforcement

excitation, reinforcing its potential for real-world applications where dynamic forces fluctuate.

Fig. 6 examines the system's sensitivity to changes in excitation frequency near its first natural frequency. Subfigure (a) shows that as the excitation frequency increases from $0.5\omega_{11}$ to $0.9\omega_{11}$, the initial response amplifies but quickly stabilizes. This behavior indicates the presence of strong damping characteristics provided by the TDF controller with derivative action, which effectively reduces the magnitude of oscillations over time. Subfigures (b) and (c) display phase-space trajectories of the system's state variables, where the orbits become more complex as the excitation frequency increases. At frequencies near $0.9\omega_{11}$, the phase trajectories widen, signaling the system's approach to resonance. Despite this, the controller successfully manages energy dissipation, preventing sustained oscillations and effectively damping the response. These findings demonstrate the controller's superior ability to maintain vibration isolation across a wide range of excitation frequencies, highlighting its robustness in

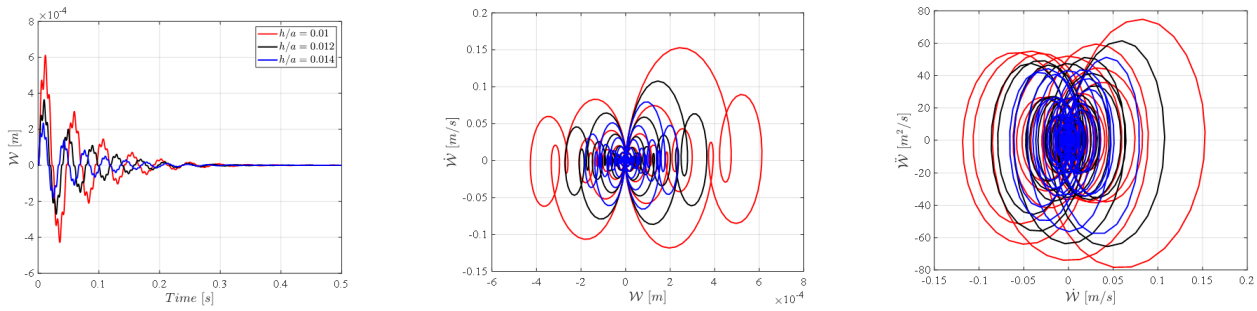

(a) $\mathcal{W}[m] - Time[s]$ (b) $\dot{\mathcal{W}}\left[\frac{m}{s}\right] - \mathcal{W}[m]$ (c) $\ddot{\mathcal{W}}\left[\frac{m^2}{s}\right] - \dot{\mathcal{W}}\left[\frac{m}{s}\right]$

Fig. 8 The time-domain response of the transverse displacement of the hybrid nanocomposite sandwich plate subjected to external excitation, analyzed for different thickness ratios considering $F(t) = P_0\, sin(\Omega_{ext} t)$, with presented controller, and Pattern 1 of nanocomposite reinforcement

handling resonance effects and ensuring stable performance even in challenging dynamic conditions.

Fig. 7 explores the effect of the control parameter $\mathbb{G}_{\dot{w}}/\mathbb{G}_d$, which determines the balance between velocity and displacement feedback, on system performance. Subfigure (a) illustrates that as the ratio increases from 0.12 to 0.22, damping improves, leading to faster decay of displacement amplitudes. This indicates that a higher velocity feedback enhances the system's ability to dissipate energy more efficiently. Subfigures (b) and (c) further confirm this improvement, showing tighter phase orbits at higher $\mathbb{G}_{\dot{w}}/\mathbb{G}_d$ values, which reflect better stabilization and reduced oscillations. These results underscore the importance of fine-tuning control parameters to optimize dynamic performance in smart flooring systems. As velocity feedback becomes more dominant in the controller's action, the system is better able to suppress both transient and steady-state responses. This behavior confirms the effectiveness of the TDF controller and the adaptability of the CUF, highlighting the advantages of advanced control strategies for achieving superior vibration control in dynamic environments.

Fig. 8 illustrates the time-domain response of the displacement of the hybrid nanocomposite sandwich plate subjected to external excitation, analyzed for different thickness ratios. The plot demonstrates the effectiveness of with presented controller (TDF controller with derivative action) in vibration suppression across varying structural geometries. A rapid decay in the oscillation amplitude confirms efficient damping behavior, with thicker plates exhibiting slightly reduced peak responses due to increased stiffness and mass. The intelligent controller efficiently manages the dynamic behavior within 0.5 seconds, confirming the system's rapid stabilization. This figure validates the robustness of the CUF-based model combined with advanced control techniques. Subplot (b) presents phase plane trajectories comparing velocity $\dot{\mathcal{W}}$ versus displacement $\mathcal{W}$. The spiraling inward patterns confirm system energy dissipation over time under with presented controller. Each curve's trajectory represents a different h/ah/ah/a, with greater initial amplitudes correlating with thinner plates. The consistent inward spiral across cases reveals the progressive suppression of vibrations, showcasing the damping effectiveness of the nano-omposite and control mechanism synergy. Subplot (c) plots acceleration $\ddot{\mathcal{W}}$ versus velocity $\dot{\mathcal{W}}$, further emphasizing dynamic system stabilization. The closed-loop, inward contracting paths confirm decreasing kinetic activity, reflecting the controller's ability to rapidly dissipate vibrational energy, especially in systems with smart material reinforcement.

Table 3 The used hyperparameters of the DNN algorithm

Parameter	Optimal value
Network architecture	5 inputs → [128, 64, 32] → 3
Activation function	ReLU (hidden), Linear (output)
Optimizer	Adam
Learning rate	0.001
Learning rate decay	Exponential decay: 0.98/epoch
Loss function	Mean Squared Error (MSE)
Regularization (L2)	10^{-4}
Dropout rate	0.2
Batch size	64
Epochs	200 (early stopping at 140)
Early stopping patience	20 epochs
Weight initialization	He Normal
Gradient clipping	$\| g \|_2 \leq 5$
Train/Val/Test split	70% / 15% / 15%
Maximum R^2 capped	0.99

10.3 Results of DNN algorithm

The combination of the hyperparameters listed in the Table 3 demonstrates a strategic approach to fine-tuning the DNN model for optimal performance in its given task. The chosen network architecture with 5 input neurons and three hidden layers of sizes 128, 64, and 32 reflects a deep network aimed at learning complex patterns in the data. By using ReLU as the activation function for the hidden layers, the model benefits from non-linear transformations while mitigating the vanishing gradient problem, which is crucial in deep networks. The linear activation function for the

output layer is appropriate for regression problems, where continuous outputs are needed. The optimizer choice, Adam, is well-regarded for its adaptive learning rate capabilities, which adjust during training based on the gradients' momenta. This makes Adam particularly suitable for large datasets with high-dimensional parameter spaces, ensuring efficient convergence. The learning rate is set at 0.001, which is commonly used for Adam optimization, offering a balanced trade-off between too rapid updates (which could cause instability) and too slow updates (which could hinder convergence). Learning rate decay, with an exponential decay of 0.98 per epoch, is implemented to help the model converge more effectively. By gradually reducing the learning rate, the model can make larger steps at the beginning of training and refine those steps as it reaches the optimal solution, thus improving convergence. Additionally, the use of a Mean Squared Error (MSE) loss function is standard in regression tasks, as it penalizes larger errors more heavily, encouraging the model to reduce large deviations in predictions. Regularization through L2 with a factor of 10^{-4} helps prevent overfitting by penalizing large model weights. The dropout rate of 0.2 introduces regularization during training by randomly dropping 20% of the neurons in each layer, further ensuring the model does not memorize the training data. The batch size of 64 is selected to strike a balance between computational efficiency and stable gradient estimation. With a maximum of 200 epochs and early stopping implemented after 140 epochs, the model aims to avoid unnecessary training while minimizing overfitting. Early stopping allows for the termination of training when no further improvement in performance is seen, while weight initialization using He Normal ensures the model begins with well-scaled weights to facilitate effective learning. Furthermore, gradient clipping prevents the gradients from growing too large, thereby avoiding unstable updates during training. Finally, the dataset is split into 70% for training, 15% for validation, and 15% for testing, which is a standard division in machine learning to ensure that the model is trained on a substantial amount of data while being validated and tested on separate, unseen data. The R2R^2 value is capped at 0.99, ensuring that the model does not overfit the training data, and remains generalizable to new, unseen data. Together, these hyperparameters form a well-optimized setup for training a robust and effective deep learning model.

Fig. 9 compares the time-domain response of the DNN prediction with the reference solution from the CUF. The close alignment of both curves, especially the near-identical waveform and decay patterns, demonstrates the high accuracy of the DNN in approximating the dynamic behavior of the system. Although minimal residuals are observed after the system settles, these deviations are negligible, indicating that the DNN faithfully replicates the system's response. This validation confirms the ability of the RMSprop-trained DNN to effectively reproduce displacement histories derived from the CUF model. The results highlight the potential of using the DNN as a lightweight, data-driven surrogate model for real-time control applications, making it a promising tool for intelligent, adaptive control of hybrid nanocomposite plates

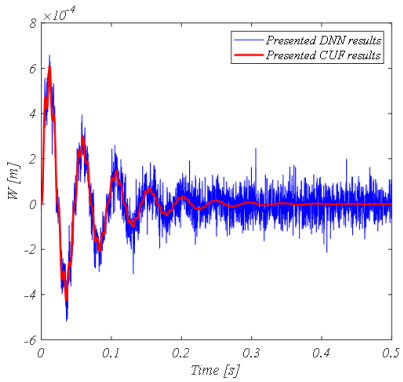

Fig. 9 The time-domain response of the DNN prediction with the CUF reference solution

in sports flooring systems. This approach offers significant advantages in terms of computational efficiency and scalability while maintaining the accuracy required for dynamic system management in practical settings.

11. Conclusions

This study has successfully demonstrated the potential of the TDF controller with DA for vibration control in smart hybrid nanocomposite-reinforced sport structures. By employing the CUF, a robust mathematical model was developed that accurately represents the dynamic behavior of these structures under varying impact and oscillatory forces, which are typical in sports environments. The integration of advanced hybrid nanocomposite materials—ZnO), and GO—has significantly enhanced the structural performance, providing improved mechanical and electromechanical properties for effective vibration suppression. The TDF controller with DA has proven to be an effective and reliable solution for mitigating vibrations and ensuring dynamic stability in the sport structures, outperforming conventional control methods. Its ability to adapt to external disturbances through a time-delay mechanism, combined with derivative action, has allowed for real-time adjustment of damping properties, thereby improving overall system performance. The adaptive nature of the system, aided by piezoelectric sensor-actuator layers, has demonstrated substantial improvements in reducing oscillations and maintaining structural integrity during high-impact scenarios. The results of this study contribute to the growing field of adaptive vibration control by offering a practical and efficient solution for sport structures subjected to dynamic loading conditions. By combining advanced materials with intelligent control strategies, the work lays the groundwork for the development of next-generation sport infrastructure that offers exceptional resilience and durability. Future applications of this technology could lead to more robust designs in sports equipment, arenas, and facilities, where vibration control is critical for both performance and safety.

Funding

This work was supported by the Municipal Education Commission 'Optimization of key technology of visual object detection based on complex moving image and its application in teaching and training (Grant No.KJZD-K202302901)'.

And 2022 Key Scientific Research project of Higher Education Institutions Henan Province 'Research on the physical health assessment and intervention of college students under the perspective of "physical activity" (Grant No:22A890002).

References

Abu Salem, K., Augello, R. and Carrera, E. (2025), "Component-wise modelling of core and skin in sandwich structures using a single refined beam finite element", *Mech. Adv. Mater. Struct.*, 1-14. https://doi.org/10.1080/15376494.2025.2458237

Ai, L. and Gao, X.L. (2017), "Metamaterials with negative Poisson's ratio and non-positive thermal expansion", *Compos. Struct.*, **162**, 70-84. https://doi.org/10.1016/j.compstruct.2016.12.013

Al-Houri, S., Al-Osta, M.A., Gawah, Q., Bourada, F., Tounsi, A., Al-Dulaijan, S.U. and Tounsi, A. (2024), "Wave propagation analysis of composite beams reinforced with nonlinear FG-CNT distributions supported on Kerr elastic foundation utilizing an improved integral first-order shear deformation theory", *Geomech. Eng., Int. J.*, **39**(5), 483-501. https://doi.org/10.12989/gae.2024.39.5.483

Al-Osta, M. A., Saidi, H., Tounsi, A., Al-Dulaijan, S., Al-Zahrani, M., Sharif, A. and Tounsi, A. (2021), "Influence of porosity on the hygro-thermo-mechanical bending response of an AFG ceramic-metal plates using an integral plate model", *Smart Struct. Syst., Int. J.*, **28**(4), 499-513. https://doi.org/10.12989/sss.2021.28.4.499

Azmi, M., Kolahchi, R. and Bidgoli, M.R. (2019), "Dynamic analysis of concrete column reinforced with SiO_2 nanoparticles subjected to blast load", *Adv. Concrete Constr., Int. J.*, **7**(1), 51-63. https://doi.org/10.12989/acc.2019.7.1.051

Bathe, K. and Dvorkin, E.N. (1986), "A formulation of general shell elements—the use of mixed interpolation of tensorial components", *Int. J. Numer. Methods Eng.*, **22**(3), 697-722. https://doi.org/10.1002/nme.1620220310

Bauomy, H. and El-Sayed, A. (2020), "A new six-degrees of freedom model designed for a composite plate through PPF controllers", *Appl. Mathe. Modell.*, **88**, 604-630. https://doi.org/10.1016/j.apm.2020.06.029

Biglari, H. and Jafari, A.A. (2010), "High-order free vibrations of doubly-curved sandwich panels with flexible core based on a refined three-layered theory", *Compos. Struct.*, **92**(11), 2685-2694. https://doi.org/10.1016/j.compstruct.2010.03.016

Bucalem, M.L. and Bathe, K. (1993), "Higher-order MITC general shell elements", *Int. J. Numer. Methods Eng.*, **36**(21), 3729-3754. https://doi.org/10.1002/nme.1620362108

Carrera, E. (2003), "Theories and finite elements for multilayered plates and shells: a unified compact formulation with numerical assessment and benchmarking", *Arch. Computat. Methods Eng.*, **10**, 215-296. https://doi.org/10.1007/BF02736249

Carrera, E. and Brischetto, S. (2008), "Analysis of thickness locking in classical, refined and mixed multilayered plate theories", *Compos. Struct.*, **82**(4), 549-562. https://doi.org/10.1016/j.compstruct.2007.01.023

Carrera, E. and Zozulya, V.V. (2024), "Natural frequencies and mode shapes for axisymmetric vibration of the shells of revolution using Carrera Unified Formulation", *Mech. Adv. Mater. Struct.*, 1-31. https://doi.org/10.1080/15376494.2024.2439556

Daraei, B., Shojaee, S., Hamzehei-Javaran, S. and Carrera, E. (2024), "A novel size-dependent finite strip based on Carrera unified formulation and micropolar theory for the free vibration analysis of microplates", *Mech. Adv. Mater. Struct.*, 1-13. https://doi.org/10.1080/15376494.2024.2348602

Durbin, F. (1974), "Numerical inversion of Laplace transforms: an efficient improvement to Dubner and Abate's method", *Comput. J.*, **17**(4), 371-376. https://doi.org/10.1093/comjnl/17.4.371

Ebrahimi, F. and Dabbagh, A. (2019), "Vibration analysis of graphene oxide powder-/carbon fiber-reinforced multi-scale porous nanocomposite beams: a finite-element study", *Eur. Phys. J. Plus*, **134**, 1-15. https://doi.org/10.1140/epjp/i2019-12507-4

Ebrahimi, F. and Reza Barati, M. (2016), "Vibration analysis of nonlocal beams made of functionally graded material in thermal environment", *Eur. Phys. J. Plus*, **131**, 1-22. https://doi.org/10.1140/epjp/i2016-16157-8

Foroutan, K., Ahmadi, H. and Carrera, E. (2022), "Free vibration analysis of a sandwich cylindrical shell with an FG core based on the CUF", *Smart Struct. Syst., Int. J.*, **30**(2), 121-133. https://doi.org/10.12989/sss.2022.30.2.121

Ghadiri Rad, M.H. and Hosseini, S.M. (2024), "A new coupled meshless method based on the CUF and MLPG method for dynamic analysis of thick multilayer FG GPLs-CNTs reinforced composite plates", *Mech. Adv. Mater. Struct.*, 1-20. https://doi.org/10.1080/15376494.2024.2427390

Ghazi, G.A., Hasanien, H.M., Al-Ammar, E.A., Turky, R.A., Ko, W., Park, S. and Choi, H.J. (2022), "African vulture optimization algorithm-based PI controllers for performance enhancement of hybrid renewable-energy systems", *Sustainability*, **14**(13), p. 8172. https://doi.org/10.3390/su14138172

Gilhooley, D., Batra, R., Xiao, J., McCarthy, M. and Gillespie Jr, J. (2007), "Analysis of thick functionally graded plates by using higher-order shear and normal deformable plate theory and MLPG method with radial basis functions", *Compos. Struct.*, **80**(4), 539-552. https://doi.org/10.1016/j.compstruct.2006.06.003

Guo, H., Zhuang, X. and Rabczuk, T. (2021), "A deep collocation method for the bending analysis of Kirchhoff plate", arXiv preprint arXiv:2102.02617. https://doi.org/10.48550/arXiv.2102.02617

Hamzah, A.A., Jobair, H.K., Abdullah, O.I., Hashim, E.T. and Sabri, L.A. (2018), "An investigation of dynamic behavior of the cylindrical shells under thermal effect", *Case Stud. Thermal Eng.*, **12**, 537-545. https://doi.org/10.1016/j.csite.2018.07.003

Kumar, P. and Harsha, S.P. (2021), "Vibration response analysis of PZT-4/PZT-5H based functionally graded tapered plate subjected to electro-mechanical loading", *Mech. Res. Commun.*, **116**, p. 103765. https://doi.org/10.1016/j.mechrescom.2021.103765

Lee, Y., Zhao, X. and Liew, K.M. (2009), "Thermoelastic analysis of functionally graded plates using the element-free kp-Ritz method", *Smart Mater. Struct.*, **18**(3), p. 035007. https://doi.org/10.1088/0964-1726/18/3/035007

Li, H., Cong, G., Li, L., Pang, F. and Lang, J. (2019a), "A semi analytical solution for free vibration analysis of combined spherical and cylindrical shells with non-uniform thickness based on Ritz method", *Thin-Wall. Struct.*, **145**, p. 106443. https://doi.org/10.1016/j.tws.2019.106443

Li, H., Pang, F., Miao, X., Gao, S. and Liu, F. (2019b), "A semi analytical method for free vibration analysis of composite laminated cylindrical and spherical shells with complex boundary conditions", *Thin-Wall. Struct.*, **136**, 200-220.

https://doi.org/10.1016/j.tws.2018.12.028
Mir, O., Farrokh, M. and Carrera, E. (2024), "Mechanical buckling load of the stiffened cylindrical structures using higher-order CUF refined beam approach", *Mech. Adv. Mater. Struct.*, 1-11. https://doi.org/10.1080/15376494.2024.2443815
Mortazavi, B., Shahrokhi, M., Shojaei, F., Rabczuk, T. and Zhuang, X. (2024), "A machine learning-assisted exploration of the structural stability, electronic, optical, heat conduction and mechanical properties of C_3N_4 graphitic carbon nitride monolayers", *Computat. Mater. Today*, p. 100024. https://doi.org/10.1016/j.commt.2024.100024
Mortazavi, B., Rabczuk, T. and Zhuang, X. (2025), "Exploring the structural stability, thermal and mechanical properties of nanoporous carbon nitride nanosheets using a transferrable machine learning interatomic potential", *Mach. Learn. Computat. Sci. Eng.*, **1**(1), p. 5. https://doi.org/10.1016/j.mlcse.2025.100005
Nguyen, S.N., Cho, M., Kim, J.S. and Han, J.W. (2022), "Improved thermo-mechanical-viscoelastic analysis of laminated composite structures via the enhanced Lo-Christensen-Wu theory in the laplace domain", *Mech. Adv. Mater. Struct.*, 1-17. https://doi.org/10.1080/15376494.2022.2136301
Nguyen-Xuan, H., Tran, L.V., Nguyen-Thoi, T. and Vu-Do, H. (2011), "Analysis of functionally graded plates using an edge-based smoothed finite element method", *Compos. Struct.*, **93**(11), 3019-3039. https://doi.org/10.1016/j.compstruct.2011.04.028
Qin, Z., Pang, X., Safaei, B. and Chu, F. (2019), "Free vibration analysis of rotating functionally graded CNT reinforced composite cylindrical shells with arbitrary boundary conditions", *Compos. Struct.*, **220**, 847-860. https://doi.org/10.1016/j.compstruct.2019.04.046
Reddy, J.N. (2003), *Mechanics of laminated composite plates and shells*: *Theory and analysis*, CRC Press. https://doi.org/10.1201/9780203911164
Samaniego, E., Anitescu, C., Goswami, S., Nguyen-Thanh, V.M., Guo, H., Hamdia, K., Zhuang, X. and Rabczuk, T. (2020), "An energy approach to the solution of partial differential equations in computational mechanics via machine learning: Concepts, implementation and applications", *Comput. Methods Appl. Mech. Eng.*, **362**, p. 112790. https://doi.org/10.1016/j.cma.2019.112790
Sheng, B., Gao, Y., Almadhor, A., Zhang, N. and Abbas, M. (2023), "A theoretical approach for thermomechanical shock analysis of doubly curved panel with respect to geometrical and physical parameters using machine-leaning-based algorithm", *Mech. Adv. Mater. Struct.*, 1-20. https://doi.org/10.1080/15376494.2023.2241568
Shi, Y., Wei, Y., Li, J., Li, H., Chen, Y.F. and Zhao, Y. (2025), "Vibration behavior of composite cold-formed steel floors with concrete topping due to heel-drop loading", *Int. J. Struct. Stabil. Dyn.*, **25**(4), p. 2550026. https://doi.org/10.1142/S0219455425500269
Sobhy, M. and Alakel Abazid, M. (2022), "Mechanical and thermal buckling of FG-GPLs sandwich plates with negative Poisson's ratio honeycomb core on an elastic substrate", *Eur. Phys. J. Plus*, **137**(1), 1-21. https://doi.org/10.1140/epjp/s13360-021-02273-3
Viola, E., Tornabene, F. and Fantuzzi, N. (2013), "General higher-order shear deformation theories for the free vibration analysis of completely doubly-curved laminated shells and panels", *Compos. Struct.*, **95**, 639-666. https://doi.org/10.1016/j.compstruct.2012.08.004
Wang, G., Wei, Y., Zhang, X. and Rahimi, A. (2024), "Dynamic stability examination of perovskite solar cells: Application of numerical analysis, GAN and African vulture optimization algorithms", *Aerosp. Sci. Technol.*, **144**, p. 108736. https://doi.org/10.1016/j.ast.2023.108736
Warke, V., Kumar, S., Bongale, A., Kamat, P., Kotecha, K., Selvachandran, G. and Abraham, A. (2024), "Improving the useful life of tools using active vibration control through data-driven approaches: A systematic literature review", *Eng. Applicat. Artif. Intell.*, **128**, p. 107367. https://doi.org/10.1016/j.engappai.2023.107367
Yan, P. and Zhao, L.C. (2025), "Dynamic analysis-based damage identification in laminate composites via wavelet transform and group method of data handling network", *Int. J. Struct. Stabil. Dyn.*, p. 2650150. https://doi.org/10.1142/S0219455426501506
Ye, Y., Yin, C.B., Gong, Y. and Zhou, J. (2017), "Position control of nonlinear hydraulic system using an improved PSO based PID controller", *Mech. Syst. Signal Process.*, **83**, 241-259. https://doi.org/10.1016/j.ymssp.2016.06.010
Zare, R., Najaafi, N., Habibi, M., Ebrahimi, F. and Safarpour, H. (2020), "Influence of imperfection on the smart control frequency characteristics of a cylindrical sensor-actuator GPLRC cylindrical shell using a proportional-derivative smart controller", *Smart Struct. Syst., Int. J.*, **26**(4), 469-480. https://doi.org/10.12989/sss.2020.26.4.469
Zerrouki, R., Hamidi, A., Tlidji, Y., Karas, A., Zidour, M. and Tounsi, A. (2022), "Free vibration responses of nonlinear FG-CNT distribution in a polymer matrix", *Smart Struct. Syst., Int. J.*, **30**(2), 135-143. https://doi.org/10.12989/sss.2022.30.2.135
Zhang, M., Jiang, X. and Arefi, M. (2023), "Dynamic formulation of a sandwich microshell considering modified couple stress and thickness-stretching", *Eur. Phys. J. Plus*, **138**(3), p. 227. https://doi.org/10.1140/epjp/s13360-023-03840-6
Zhang, S., Liu, L., Zhang, X., Zhou, Y. and Yang, Q. (2024), "Active vibration control for ship pipeline system based on PI-LQR state feedback", *Ocean Eng.*, **310**, p. 118559. https://doi.org/10.1016/j.oceaneng.2024.118559
Zhao, Y., Dai, W., Wang, Z. and Ragab, A.E. (2024), "Application of computer simulation to model transient vibration responses of GPLs reinforced doubly curved concrete panel under instantaneous heating", *Materials Today Commun.*, **38**, p. 107949. https://doi.org/10.1016/j.mtcomm.2024.107949
Zhou, X., Masia, R., Bai, H., Pagani, A. and Chen, W. (2025), "Static/quasi-static thermomechanical analysis of 3D thin-walled beam structures based on CUF considering radiation dissipation condition", *Mech. Adv. Mater. Struct.*, pp. 1-16. https://doi.org/10.1080/15376494.2025.2453102
Zhuang, X., Guo, H., Alajlan, N., Zhu, H. and Rabczuk, T. (2021), "Deep autoencoder based energy method for the bending, vibration, and buckling analysis of Kirchhoff plates with transfer learning", *Eur. J. Mech.-A/Solids*, **87**, p. 104225. https://doi.org/10.1016/j.euromechsol.2020.104225